# In-Cloud Icing - A case study at Fagernesfjellet, Norway using Weather Research and Forecasting model and observations.

*Pravin Punde[1], Yngve Birkelund[1], Muhammad Shakeel Virk[1], Xingbo Han[1]*

[1] *UiT The Arctic University of Norway*

pravin.b.punde@uit.no, yngve.birkelund@uit.no, muhammad.s.virk@uit.no, xingbo.han@uit.no

*Abstract*— **Atmospheric icing poses significant challenges to infrastructure integrity and transportation safety, especially in mountainous regions such as Fagernesfjellet, Norway. This paper presents a comprehensive case study of in-cloud icing over Fagernesfjellet, leveraging hindcast data obtained through dynamic downscaling with the Weather Research and Forecasting (WRF) model alongside observational data. Spanning from October 1, 2022, to December 31, 2022, the study focuses on evaluating the performance of microphysical schemes in predicting icing rates, liquid water content and other hydrometeors. Various statistical analyses are employed to assess model accuracy and validate against field measurements. The findings highlight the proficiency of the WRF model in simulating in-cloud icing, with the Thompson scheme exhibiting better performance in replicating low icing rates threshold compared to alternative schemes while Morrison for high icing rates threshold. This study underscores the critical role of model physics selection in accurately assessing in-cloud icing conditions, offering valuable insights for icing prediction and infrastructure resilience efforts. Additionally, we utilize NEWA data to analyse icing climate from 2005 to 2018, and further validate WRF results against NORA3 data over a three-month simulation period.**

Keywords— ***ice accretion, NWP model for icing, ice load, microphysics, in- Cloud Icing, atmospheric icing, icing, WRF***

## I. Introduction

In-cloud icing, occurring when unheated structures encounter liquid cloud droplets at temperatures below freezing, is particularly prevalent in exposed mountainous regions where cloud bases often descend below peak elevations. This phenomenon, lasting days or even weeks in some areas, poses significant risks to infrastructure integrity, including power lines, wind turbines, and telecommunication towers[1]. Ski lifts, measurement masts, and buildings are also susceptible, with instances of ice accumulation exceeding 300 kg/m² reported [2]. Reliable long-term icing data is scarce, but crucial for assessing icing climatology, especially in Nordic regions where potential wind farm sites are frequently subject to in-cloud icing [3]. The impact on wind power production can be substantial, emphasizing the need for robust modelling tools to evaluate icing frequency and intensity. In-cloud icing also poses safety hazards for small aircraft, necessitating further attention and mitigation strategies [4].

Utilizing the Weather Research and Forecasting (WRF) model, our research focuses on investigating in-cloud icing phenomena at Fagernesfjellet. Our aim was twofold: to analyse the specific in-cloud icing conditions experienced at Fagernesfjellet and to evaluate the effectiveness of various microphysics schemes within the WRF model. To establish a climatological perspective, we integrated data from the New European Wind Atlas (NEWA) [5]. Furthermore, we validated the WRF model outcomes through comparison with both observational data and the NORA3 dataset [6].

## II. Data and Methods

### A. Study Area

Fagernesfjellet (68.4206° N 17.4851° E), located on Norway's western coast, is 1013 meters above sea level and lies to the east of the Ofotfjorden and northwest of the Beisfjorden. This region has a diverse and complex mountainous topography, which is distinguished by its proximity to the Arctic Circle and location near the Swedish national border. Fagernesfjellet faces the open sea to the south, spreading southwest and westward. The air masses that sweep across this area are moist, owing to the Gulf Stream currents running through the North Atlantic Ocean, which contribute to atmospheric ice occurrences during the winter. With air temperatures ranging from -21°C to 0°C, conditions are favourable for atmospheric icing, which shapes the region's peculiar environment [7].

Fagernesfjellet test site was established in October 2022. In addition to measuring wind speed, wind direction, and air temperature, it provides ice load on a cylinder with minute resolution.


Fig. 1 Location of the Fagernesfjellet test site [8]

### B. Datasets

The NEWA dataset, developed in collaboration with the Technical University of Denmark (DTU) and other European institutions, provides comprehensive wind resource information tailored specifically for Europe. With a spatial resolution of 3 km, NEWA offers detailed data on icing, winds, and related parameters spanning from 2005 to 2018. In

our study, we utilized NEWA data to analyse the climatology of icing, precipitation, wind, and temperature at 2 meters above the ground (T2m) over our study location. The dataset, available at half-hourly resolution, includes icing loads measured at heights ranging from 50 to 500 meters, with our analysis focusing on the lowest level. We converted icing loads to the number of icing days and precipitation to annual values, while dividing wind speed data into seasonal categories (winter, spring, summer, autumn) to identify prevailing wind directions during specific seasons. T2m data was retained in its original temporal resolution for further analysis.

The NORA3 dataset is a high-resolution, nonhydrostatic hindcast covering the North Sea, Norwegian Sea, Barents Sea, and the Scandinavian Peninsula. Spanning from 1995 to 2020, NORA3 provides a detailed three-dimensional representation of the atmosphere. Utilizing a horizontal resolution of 3 km, NORA3 incorporates surface analysis and boundary conditions from ERA5, a global reanalysis dataset. In our analysis, we utilized NORA3 data for T2m, relative humidity (RH), wind speed, and direction, retaining these variables in their native temporal resolution. We compared NORA3 data with observations and outputs from the Weather Research and Forecasting (WRF) model to assess its performance.

### C. Model Configuration

We employed the fully compressible nonhydrostatic Advanced WRF model (Version 4.4) [9] for simulating october 1st, 2022 to December 31st, 2022. The model utilized terrain-following coordinates with a constant pressure top surface. The model configuration leveraged the Global Multi-resolution Terrain Elevation Data 2010 (GMTED 2010) with horizontal resolution 30 arc-seconds (1km) is used as terrain input data.

We configured WRF with one-way nested domains: a 9 km outer domain (D01) and a 3 km second domain (D02) and 1 km 3rd domain (D03). All three domains spanned from the surface up to 50 hPa with 51 vertical levels. The domain setup can be seen in fig. 2.

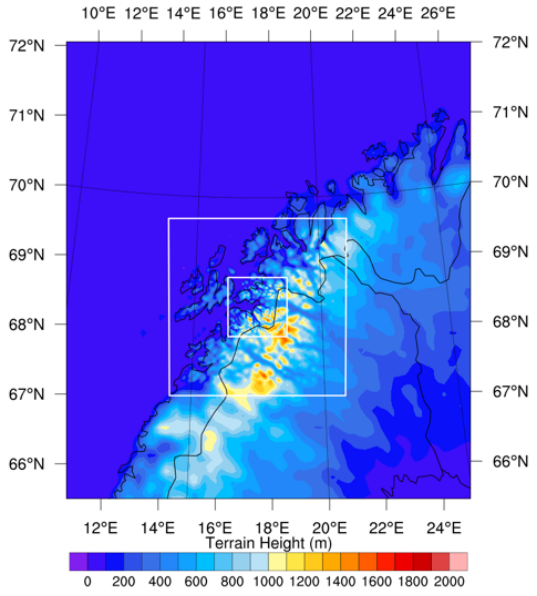


Fig. 2 WRF Domain setup. Colours represents terrain heights within the domain.

### A. Initial and Boundary Conditions

Initial and lateral boundary conditions, along with sea surface temperature data, were obtained from the European Centre for Medium-Range Weather Forecasts Atmospheric Reanalysis of the Global Climate (ERA5 ) [10].

### B. Parameterization Schemes

TABLE I. WRF MODEL SETUP

| | |
|---|---|
| Initial, lateral boundary condition | ECMWF Atmospheric Reanalysis of the Global Climate (ERA5) (0.25°) |
| Domain extends | 9°E – 27°E, 65°N –72°N |
| Radiation schemes (Shortwave, Longwave) | Rapid Radiative Transfer Model for global circulation models (RRTMG) [11] |
| Planetary boundary layer Scheme | YSU [12] |
| Land surface scheme | Noah land surface model scheme[13] |

A detailed breakdown of the various parameterization schemes employed in the model simulations is provided in Table I. Here, we'll highlight a microphysics choices.

The Thompson scheme [14] scheme explicitly predicts the mixing ratios of various hydrometeors, including cloud water, rain, graupel, cloud ice, and snow. It utilizes a double-moment approach for cloud ice, predicting both the mass and number concentration of ice particles. Milbrandt-Yau 2-Moment Scheme (Milbrandt) [15] scheme predicts both the mass mixing ratio and the number concentration for all six hydrometeor species: cloud water, rain, cloud ice, snow, graupel, and hail. Morrison Double-Moment scheme [16] predicts the mass mixing ratio and number concentration of major hydrometeors that influence precipitation, including ice, snow, rain, and graupel. WRF Single-Moment 6-class (WSM6) [17] forecasts simply the mass mixing ratio for different hydrometeors to maximize computing efficiency. WRF Double-Moment 7-class (WDM7) [18] is a variation of WSM6 that adds graupel as a separate category and provides double-moment prediction for warm rain processes (cloud water and rain).

### D. Ice accretion model

The International Organization for Standardization (ISO) established a model for ice accretion known as the Makkonen model [19]. Ice accumulation principles are modeled using a Standard Reference Collector, a cylindrical device with a rotating circular cross-section. Typically 30 mm in diameter and 1 meter in length, it can be shortened to 500 mm for scenarios with significant ice buildup [2] .This collector serves as the basis for ice accretion rate calculations. The model's calculations estimate the ice accretion rate using

$$\frac{dM}{dt} = \alpha_1 . \alpha_2 . \alpha_3 . v . A . LWC \qquad (1)$$

Where $\frac{dM}{dt}$ is the ice accretion mass ($kg/s$), $\alpha_1$= collision efficiency, $\alpha_2$= sticking efficiency, $\alpha_3$= freezing efficiency, $v$ = wind speed($m/s$), $A$ = Area of cross section($m^2$), $LWC$= liquid water content ($kg/m^2$).

Ice accumulation rate (dM/dt) depends on collision efficiency (α1), sticking efficiency (α2), freezing efficiency (α3), wind speed (v), object's cross-sectional area (A), and

liquid water content (LWC) in the air. Collision efficiency (α1) reflects droplets hitting the object, while sticking efficiency (α2) determines how many sticks, and freezing efficiency (α3) influences ice growth. Higher wind speed (v) increases droplet contact, and the object's cross-sectional area (A) affects the available surface for ice accumulation. LWC dictates the available water to freeze. [20] proposed the Median Volume Diameter method for collision efficiency, simplifying calculations while maintaining accuracy. This approximation offers a valuable tool for practical applications, as supported by [21].

The MVD can be calculated as follows.

$$MVD = \frac{(3.672+\mu)}{\lambda} \quad (2)$$

Where $\mu$ = shape parameter depends on droplet number concentration $N_c$ ($cm^{-3}$)

$\mu$ can be calculated as

$$\mu = \min\left(\frac{1000}{N_c} + 2{,}15\right) \quad (3)$$

also $\lambda$ can be calculated using.

$$\lambda = \left[\frac{\pi}{6}\rho_w \left(\frac{\Gamma(4+\mu)}{\Gamma(1+\mu)}\right)\left(\frac{N_c}{LWC}\right)\right]^{\frac{1}{3}} \quad (4)$$

Where $\rho_w$ = density of water ($kg/m^2$)

$\alpha_1$ can be caculated using MVD

$$\alpha_1 = A - 0.028 - C(B - 0.0454) \quad (5)$$

Where,

$$A = 1.066K^{-0.00616}\exp(-1.103K^{-0.688})$$
$$B = 3.641K^{-0.498}\exp(-1.497K^{-0.694})$$
$$C = 0.00637(\phi - 100)^{0.381}$$

Where K = Droplet Inertia Parameter, $\phi$ = Langmuir parameter [22], they can be calculated using

$$K = \frac{\rho_w MVD^2 v}{9\mu D}$$
$$\phi = \frac{\rho_a MVDv}{u}$$

Where D is the cylinder diameter, $R_e$= Reynolds number

$\rho_a$= Air density($kg/m^3$), $u$ = dynamic viscosity($kg/m.s$), $v$ = free stream velocity($m/s$).

*B. Model verification.*

To evaluate the model simulations, a range of statistical metrics were calculated for WRF and NORA3, including mean bias, root-mean-square error (RMSE), Bias(B), and the Pearson correlation coefficient (PCC). These metrics provide essential quantitative insights into the performance and accuracy of the model simulations.

$$RMSE = \sqrt{\frac{\sum_{i=1}^{n}(x_i - o_i)^2}{n}} \quad (6)$$

$x_i$ and $o_i$ are the model and observed variable for i[th] point. n is the total number of points.

$$B = \frac{1}{n}\sum_{i=1}^{n}(x_i - o_i) \quad (7)$$

$$PCC = \frac{COV(x_i, o_i)}{\sigma x_i \, \sigma o_i} \quad (8)$$

$COV(x_i, o_i)$ is the covariance between $x_i$ and $O_i$ (model and observed variables, respectively) Here $\sigma x_i$ and $\sigma o_i$ are the standard deviation of variable for model and observation, respectively.

Probability of Detection (POD) and False Alarm Ratio (FAR) are essential metrics used to assess the performance of predictive models in accurately predicting weather events. The POD measures the percentage of observed events that were correctly predicted by the model, providing a straightforward indication of predictive accuracy. On the other hand, the FAR evaluates the model's tendency to incorrectly forecast events that do not occur, offering insights into potential false predictions.

POD is computed by dividing the total number of observed events correctly identified by the model, known as "hits," by the total number of observed events. With a scale ranging from 0 to 1, a POD score of 1 signifies perfect accuracy [23].

$$POD = \frac{H}{M+H} \quad (9)$$

FAR is calculated by dividing the number of false alarms by the total number of forecasted events. With a scale ranging from 0 to 1, a FAR score of 0 indicates perfect accuracy, meaning no false alarms were raised by the model. Essentially, the FAR provides a straightforward measure of the model's tendency to predict an event when none actually occurred, offering valuable insight into its reliability and performance.[23]

$$FAR = \frac{F}{F+H} \quad (10)$$

## III. Results and Discussion

### A. *Icing, precipitation, temperature and wind climatology*

The location at Fagernesfjellet, as indicated by data from NEWA, experiences an annual occurrence of icing days ranging between 125 and 175 within the period from 2005 to 2018; can be seen in fig. 3. While there appears to be a decreasing trend in icing days over this timeframe, it is not deemed statistically significant. Despite this, the region remains susceptible to icing events, underscoring its vulnerability to atmospheric icing phenomena.

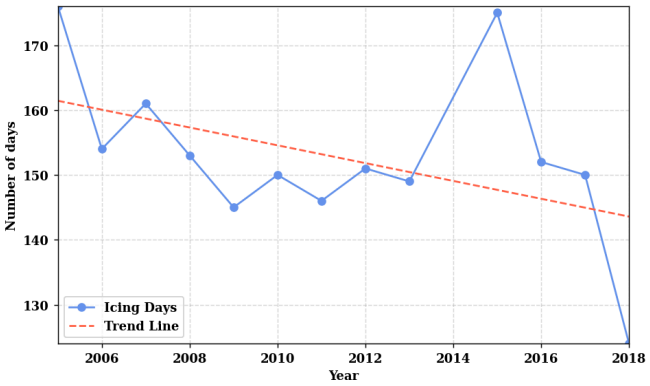


Fig. 3 Number of Icing days climatology at Fagernesfjellet between years 2005-2018.

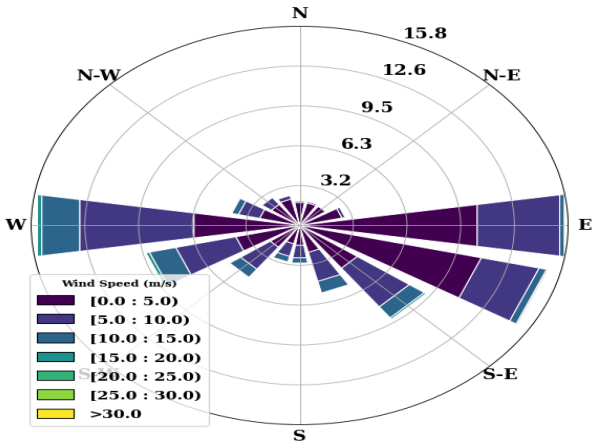


Fig. 4 Wind climatology at Fagernesfjellet between years 2005-2018.

In addition to icing events, the total precipitation climatology reveals that Fagernesfjellet receives an annual precipitation range of 1280 to 2200 millimetres (not shown in figure). Notably, there is also a trend of decreasing total precipitation over time, although, similar to the number of icing days trend, this decrease is not statistically significant. This data further underscores the area's susceptibility to both icing and precipitation occurrences, highlighting the importance of continued monitoring and assessment of icing patterns in the region.

Annually the prevailing wind directions are west, east, and south-east as shown in fig. 4. The annual maximum wind speed observed was 23 m/s and. During the winter season (DJF) (not shown in figure), the prevailing wind direction is predominantly from the east to southeast, reaching maximum speeds of approximately 26 m/s and mean 6 m/s. Conversely, in the transition months of spring (MAM) (not shown in figure), the wind direction shifts to east-southeast to west-southwest, with peak speeds reaching around 19 m/s and mean 5 m/s. Throughout the summer season (JJA) (not shown in figure), winds primarily originate from the west, with maximum wind speeds peaking at 17 m/s and mean 4 m/s. As autumn arrives (SON) (not shown in figure), the dominant wind patterns feature westerly and east-south-easterly directions, with peak wind speeds again reaching around 25 m/s and mean 5 m/s. The T2m climatology reveals a broad range of temperature values, spanning from -21°C during winter to 25°C on summer days, as shown in fig. 5.

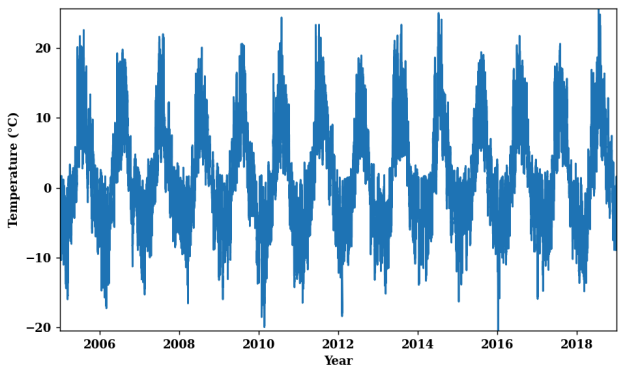


Fig. 4 T2m climatology at Fagernesfjellet between years 2005-2018.

B. *Comparative Analysis of Meteorological Parameters from Observations, NORA3, and WRF for October-December 2022*

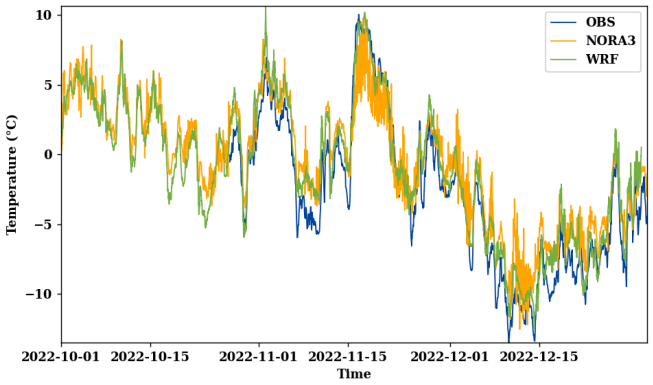


Fig. 6 T2m at Fagernesfjellet between Oct-Dec 2022 from Observations, NORA3, WRF.

The fig. 6 depicts the observed and simulated T2m at Fagernesfjellet. Throughout the three-month period, temperatures fluctuate between 10°C and -15°C. Both models effectively capture these temperature variations, albeit displaying slightly warmer surface temperatures compared to observations. Notably, the WRF results closely align with the observed temperatures. Regarding RH, both models accurately capture the RH variations, albeit exhibiting higher RH values compared to observations. However, the disparity between WRF and observations is less pronounced compared to NORA3, fig. 7 reports the Relative Humidity Comparison. The prevailing wind direction during the study period was south-southeast, with the wind rose from WRF closely resembling observations compared to NORA3. Additionally, while the observed wind maxima were 20.7, WRF and NORA3 depict 25.2 and 18.3, respectively, as illustrated in the fig. 8.

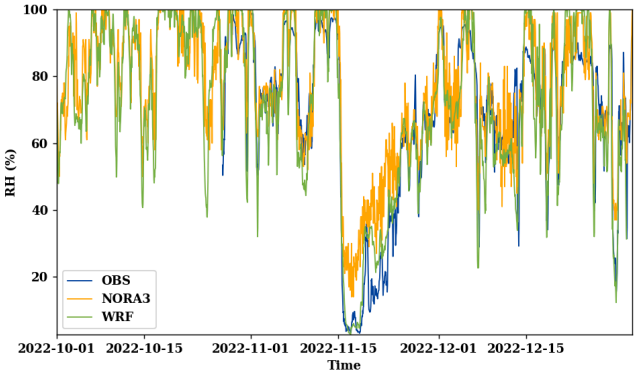


Fig. 7 Relative Humidity Comparison at Fagernesfjellet during Oct-Dec 2022 from Observations vs. NORA3 vs. WRF.

During the three-month period, statistical analysis reveals notable performance metrics for T2m, RH, and wind speed for both WRF and NORA3 models. In terms of T2m, WRF demonstrates a high correlation of 0.97, with NORA3 closely trailing at 0.94. The RMSE for WRF stands at 1.68°C, whereas NORA3 exhibits a slightly higher RMSE of 2.31°C. The B in T2m is 1.12°C for WRF and 1.44°C for NORA3. Similarly, for RH, both models show commendable correlation coefficients, with WRF at 0.90 and NORA3 at 0.91. The RMSE for RH is 11.35% for WRF and 11.74% for NORA3, with biases of -1.09% and 4.81%, respectively.

Regarding wind speed, WRF achieves a correlation of 0.66, while NORA3 registers 0.58. WRF's RMSE for wind speed is 3.74, slightly higher than NORA3's 3.56. The bias for wind speed is minimal for WRF (0.06) but slightly negative for NORA3 (-0.84). These findings are summarized in the table II.

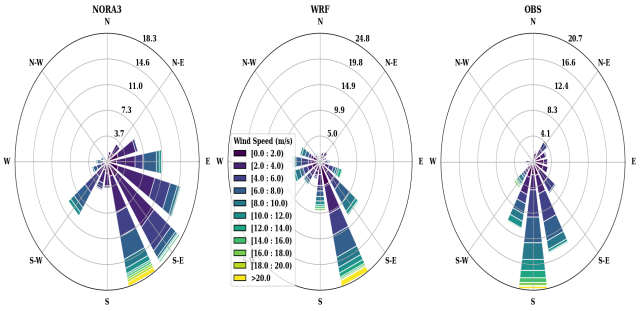


Fig. 8 Comparison of Wind Roses at Fagernesfjellet from Observations, NORA3, and WRF during Oct-Dec 2022

C. *Case study of icing event 28.10.2022 to 3.11.2022*

During the period from October 28, 2022, to November 3, 2022, we observed several icing episodes of notable intensity. To analyse these events, we employed various microphysics schemes while maintaining consistency in all other model physics settings. Observation data provided detailed icing load information on a minute-by-minute basis, which we converted into icing rates. For our analysis, we focused on instances with positive icing rates, aggregating these into hourly mean values. In contrast, the WRF model generated icing rates every 10 minutes, which we similarly consolidated into hourly means. The peak icing rate recorded during this event reached 400 g/hr, as per observational data, with the most significant icing occurring on October 28 and October 30.

TABLE III. CORRELATION, BIAS AND RMSE FOR WRF AND NORA3

| Metric | WRF -TMP | NORA3-TMP |
|---|---|---|
| Correlation | 0.97 | 0.94 |
| RMSE | 1.68 | 2.31 |
| Bias | 1.12 | 1.44 |
| | WRF-RH | NORA3-RH |
| Correlation | 0.90 | 0.91 |
| RMSE | 11.35 | 11.74 |
| Bias | -1.09 | 4.81 |
| | WRF -WS | NORA3 -WS |
| Correlation | 0.66 | 0.58 |
| RMSE | 3.74 | 3.56 |
| Bias | 0.06 | -0.84 |

The icing event coincided with distinct low-pressure systems situated over the Norwegian Sea and Russia. A notable synoptic condition on October 29, 2022, at 06 UTC, highlighted these phenomena: a low-pressure area was located in the Norwegian Sea, north of Norway, and another over Russia, moving towards Scandinavia. Fig. 9 shows the three hourly accumulated precipitation and Sea level pressure on 29.10.2022, 06 UTC. These conditions fostered strong winds in northern Norway, with maximum speeds observed between 35-40 knots. The interaction between these winds and the prevailing sea-level pressure is depicted in the fig. 10, illustrating the dynamic atmospheric conditions that might have contributed to the observed icing episodes.

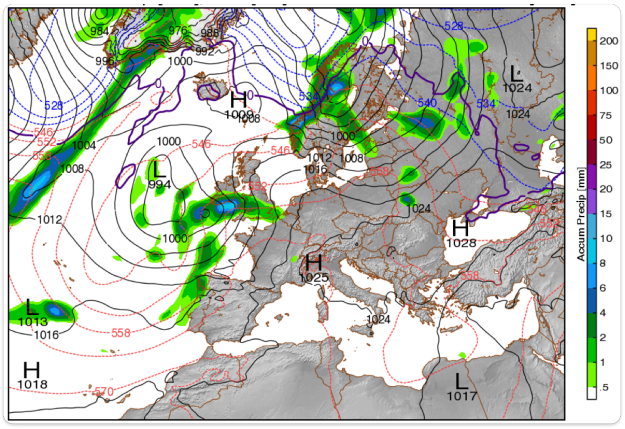


Fig. 9 Three hourly accumulated precipitation and Sea level pressure on 29.10.2022, 06 UTC from MERRA2 [24]

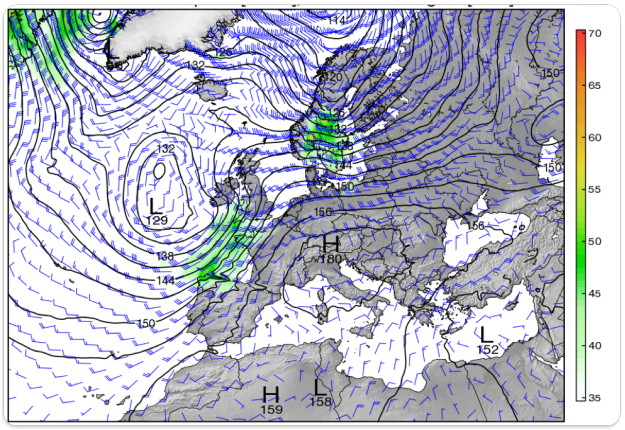

Fig. 10 850 hpa wind speed (knots) and barbs on 29.10.2022, 06 UTC from MERRA2 [24]

The LWC is a crucial parameter for understanding icing conditions. On October 29, 2022, at 06:00 UTC, the model indicates a significant presence of LWC in the lower levels, as depicted in the fig. 11(The cross section was taken along a line as shown by arrow in fig. 1). Observations reveal LWC values exceeding 0.5 g/kg at the summit of Fagernesfjellet. Moreover, a substantial amount of LWC extends up to a height of 1.5 km during this specific time interval.

In addition, the fig. 11 illustrates a notably higher concentration of LWC on the Fagernesfjellet summit compared to surrounding mountain, suggesting a possible influence of orographic lifting. At the mountain peak, the temperature hovered around zero degrees celsius, while the RH reached 99%, as evident from the figure.

Between October 28th and 30th, 2022, Fagernesfjellet experienced its highest icing rates, with observations reporting a maximum of around 400 g/hr. Various microphysics schemes generally agree with the observations but show some overestimates and underestimates. The WDM7 and Morrison schemes recorded the highest icing rates, reaching up to 420 g/hr. However, there are discrepancies in the timing of icing

rate occurrences between the actual observations and different microphysics schemes, which can be seen fig. 12.

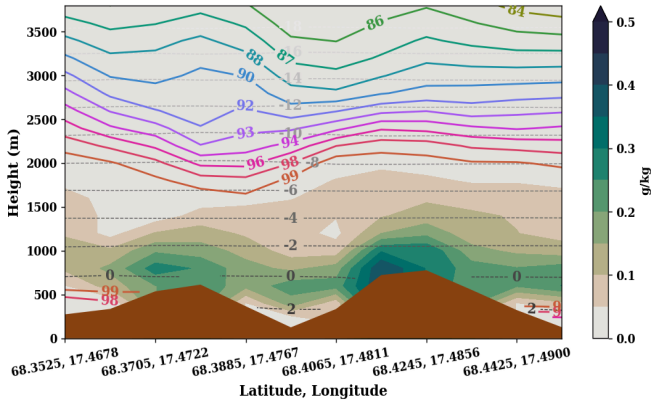


Fig. 11 Cross-sectional representation of RH, Temperature, and LWC on October 29, 2022, at 06:00 UTC from WRF.

We conducted an analysis of the Probability of Detection (POD) and False Alarm Ratio (FAR) for the icing rates. When the icing rate threshold was set at 10 g/hr, the microphysics schemes exhibited varying performance metrics. The Thompson scheme showed the highest Probability of Detection (POD) at 0.81, indicating its superior ability to accurately detect icing rates at lower thresholds. Following closely, the WSM6, Thompson, and Morrison schemes all displayed strong performance, with POD values of 0.78 each. Conversely, the WDM7 scheme showed a relatively lower POD of 0.78 and a False Alarm Ratio (FAR) of 0.50, suggesting a higher rate of false alarms compared to other schemes.

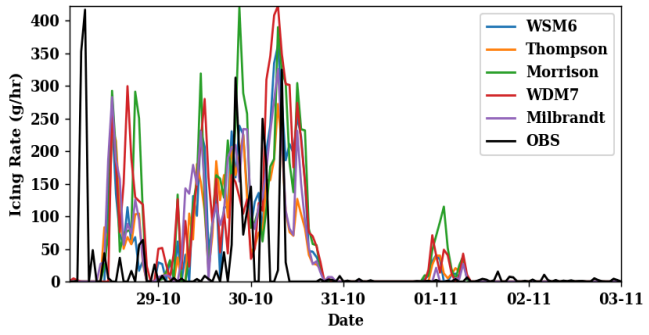


Fig. 12 Comparison of icing rates from various microphysics schemes in WRF and observations during the period from October 28, 2022, to November 3, 2022, at Fagernesfjellet.

When the icing rate threshold was increased to 50 g/hr, the performance metrics of the microphysics schemes shifted. The Morrison scheme exhibited the highest POD at 0.42, indicating its ability to accurately detect icing events at higher thresholds. The WSM6 and Thompson schemes also showed strong performance, with POD values of 0.28 each. However, the WDM7 scheme displayed a POD of 0.00, suggesting a failure to detect any icing events at the higher threshold. Additionally, the FAR values for all schemes decreased compared to the 10 g/hr threshold, indicating a reduction in false alarms. These results highlight the impact of threshold selection on the performance of microphysics schemes in detecting icing events. Details about it can be seen in table III.

TABLE IV. POD AND FAR FOR DIFFERENT MICROPHYSICS SCHEMES FOR THE ICING EVENT

| Microphysics | POD | FAR |
|---|---|---|
| Threshold 10 g/hr | | |
| WSM6 | 0.78 | 0.41 |
| Thompson | 0.81 | 0.42 |
| Morrison | 0.78 | 0.47 |
| WDM7 | 0.78 | 0.50 |
| Milbrandt | 0.78 | 0.39 |
| Threshold 50 g/hr | | |
| WSM6 | 0.28 | 0.87 |
| Thompson | 0.28 | 0.77 |
| Morrison | 0.42 | 0.82 |
| WDM7 | 0.32 | 0.71 |
| Milbrandt | 0.28 | 0.85 |

By qualitatively analysing the hydrometeor evolution in the lower atmosphere across various microphysics schemes, distinct characteristics emerge (not shown in figure). Notably, Milbrandt and Thompson schemes exhibit higher LWC, while Morrison scheme portrays the highest snow water content and WDM7 the lowest. Regarding rainwater mixing ratio, WDM7 tops the list, whereas Milbrandt records the lowest values. WDM7 also predicts the highest ice mixing ratio, followed by WSM, with other schemes showing negligible amounts. Graupel content is notably higher in the Milbrandt scheme. In summary, LWC, rainwater, and snow emerge as the dominant hydrometeors across the analysed schemes. The sample distribution of hydrometeors at lowest level from Thompson scheme is shown in fig. 13.

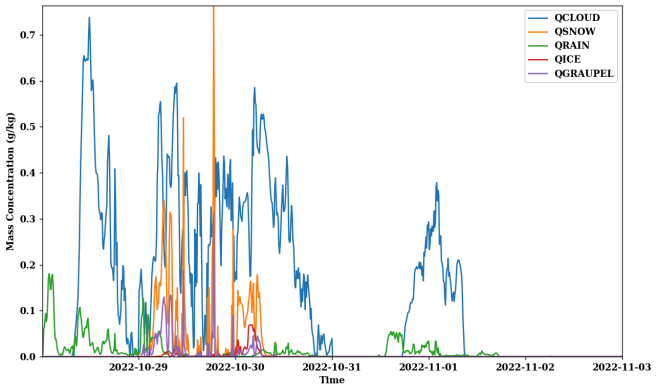


Fig. 13 Comparison of different hydrometeors from Thompson microphysics schemes in WRF during the period from October 28, 2022, to November 3, 2022, at Fagernesfjellet

## IV. Conclusions

The climatological analysis of weather parameters at Fagernesfjellet underscores the region's susceptibility to atmospheric icing and precipitation events. According to data from NEWA, the area experiences an annual occurrence of icing days ranging from 125 to 175 within the period from 2005 to 2018. Although a decreasing trend in icing days is observed over this timeframe, it is not statistically significant, emphasizing the persistent vulnerability to icing phenomena in the region. Concurrently, Fagernesfjellet receives an annual precipitation range of 1280 to 2200 millimetres, with a decreasing trend in total precipitation over time. Despite the lack of statistical significance in these trends, the findings highlight the area's continued susceptibility to both icing and precipitation occurrences.

Furthermore, the analysis of meteorological parameters from observations, NORA3, and WRF models for October to December 2022 provides valuable insights into model performance and atmospheric conditions. Both models effectively capture temperature variations, albeit exhibiting slightly warmer surface temperatures compared to observations. WRF results closely align with observed temperatures, while discrepancies in relative humidity are less pronounced in WRF compared to NORA3. Additionally, WRF demonstrates higher correlation coefficients and lower biases for temperature, relative humidity, and wind speed compared to NORA3.

During a notable icing event from October 28 to November 3, 2022, several episodes of significant icing were observed at Fagernesfjellet. The comparison of icing rates from various microphysics schemes in WRF and observations highlights some discrepancies in the timing and magnitude of icing events. Analysis of the POD and FAR for different microphysics schemes further underscores the impact of threshold selection on the detection of icing events. Notably, the Thompson scheme exhibits slightly better performance at lower icing rate thresholds, while the Morrison scheme shows better performance at higher thresholds.

Overall, these findings emphasize the importance of selection of microphysics and model physics significantly influences the determination of icing conditions, underscoring its importance in accurately assessing weather phenomena.

## Acknowledgment

The work reported in this paper is supported by nICE project (Project no- 324156) funded by UiT & Research Council of Norway. The simulations were performed on resources provided by Sigma2 – The National Infrastructure of High-Performance Computing and Data Storage in Norway.

## References

[1] Thorkildson, R., K. Jones, and M. Emery, *In-cloud icing in the Columbia basin.* Mon. Wea. Rev., 2009. **137**: p. 4369-4381.

[2] Fikke, S.M., J.E. Kristjánsson, and B.E. Kringlebotn Nygaard, *Modern Meteorology and Atmospheric Icing*. Dordrecht: Springer Netherlands: Dordrecht. p. 1-29.

[3] Kjersem, H.A., *Estimation of production losses due to icing on wind turbines at Kvitfjell wind farm*. 2019, Norwegian University of Life Sciences, Ås.

[4] Gent, R.W., N.P. Dart, and J.T. Cansdale, *Aircraft icing.* Philos. Trans. Math. Phys. Eng. Sci., 2000. **358**: p. 2873-2911.

[5] Hahmann, A.N., et al., *The making of the New European Wind Atlas – Part 1: Model sensitivity.* Geosci. Model Dev., 2020. **13**(10): p. 5053-5078.

[6] Solbrekke, I.M., A. Sorteberg, and H. Haakenstad, The 3 km Norwegian reanalysis (NORA3) – a validation of offshore wind resources in the North Sea and the Norwegian Sea. Wind Energ. Sci., 2021. **6**(6): p. 1501-1519.

[7] Rashid, T., et al., *A Field Study of Atmospheric Icing Analysis in a Complex Terrain of the High North.* The International Journal of Ocean and Climate Systems, 2014. **5**(4): p. 189-197.

[8] Norgeskart available: https://www.norgeskart.no/

[9] Skamarock, W.C., et al., *A description of the advanced research WRF version 3.* NCAR technical note, 2008. **475**: p. 113.

[10] Hersbach, H., et al., *The ERA5 global reanalysis.* Quarterly Journal of the Royal Meteorological Society, 2020. **146**(730): p. 1999-2049.

[11] Iacono, M.J., et al., *Radiative forcing by long‐lived greenhouse gases: Calculations with the AER radiative transfer models.* Journal of Geophysical Research: Atmospheres, 2008. **113**(D13).

[12] Hong, S.Y., *A new stable boundary‐layer mixing scheme and its impact on the simulated East Asian summer monsoon.* Quarterly Journal of the Royal Meteorological Society, 2010. **136**(651): p. 1481-1496.

[13] Chen, F. and J. Dudhia, Coupling an advanced land surface–hydrology model with the Penn State–NCAR MM5 modeling system. Part I: Model implementation and sensitivity. Monthly weather review, 2001. **129**(4): p. 569-585.

[14] Thompson, G., et al., *Explicit Forecasts of Winter Precipitation Using an Improved Bulk Microphysics Scheme. Part II: Implementation of a New Snow Parameterization.* Monthly weather review, 2008. **136**(12): p. 5095-5115.

[15] Milbrandt, J.A. and M.K. Yau, *A multimoment bulk microphysics parameterization. Part I: Analysis of the role of the spectral shape parameter.* Journal of the atmospheric sciences, 2005. **62**(9): p. 3051-3064.

[16] Morrison, H., J.A. Curry, and V.I. Khvorostyanov, *A new double-moment microphysics parameterization for application in cloud and climate models. part I: Description.* Journal of the atmospheric sciences, 2005. **62**(6): p. 1665-1677.

[17] Hong, S.Y. and J.-O.J. Lim, *The WRF Single-Moment 6-Class Microphysics Scheme (WSM6).* Asia-pacific Journal of Atmospheric Sciences, 2006. **42**: p. 129-151.

[18] Bae, S.Y., S.-Y. Hong, and W.-K. Tao, *Development of a single-moment cloud microphysics scheme with prognostic hail for the Weather Research and Forecasting (WRF) model.* Asia-Pacific Journal of Atmospheric Sciences, 2019. **55**: p. 233-245.

[19] Foder, M.H. *ISO 12494" Atmospheric Icing of Structures" and How to Use It*. in *ISOPE International Ocean and Polar Engineering Conference*. 2001. ISOPE.

[20] Finstad, K.J., E.P. Lozowski, and L. Makkonen, *On the median volume diameter approximation for droplet collision efficiency.* Journal of the atmospheric sciences, 1988. **45**(24): p. 4008-4012.

[21] Thornes, J.E. and D.B. Stephenson, *How to judge the quality and value of weather forecast products.* Meteorological Applications, 2001. **8**(3): p. 307-314.

[22] Global Modelling and assimilation office, 2024.

Online: https://gmao.gsfc.nasa.gov/